Michigan Tech Publications, Part 2

1-17-2024

Galactic Gamma-Ray Diffuse Emission at TeV Energies with HAWC Data

R. Alfaro
Universidad Nacional Autónoma de México

C. Alvarez
Universidad Autónoma de Chiapas

J. C. Arteaga-Velázquez
Universidad Michoacana de San Nicolás de Hidalgo

K. P. Arunbabu
St. Albert's College

D. Avila Rojas
Universidad Nacional Autónoma de México

See next page for additional authors

Recommended Citation

Authors

R. Alfaro, C. Alvarez, J. C. Arteaga-Velázquez, K. P. Arunbabu, D. Avila Rojas, R. Babu, and et al.

Galactic Gamma-Ray Diffuse Emission at TeV Energies with HAWC Data

R. Alfaro[1], C. Alvarez[2], J. C. Arteaga-Velázquez[3], K. P. Arunbabu[4], D. Avila Rojas[1], R. Babu[5], V. Baghmanyan[6],
E. Belmont-Moreno[1], C. Brisbois[7], K. S. Caballero-Mora[2], T. Capistrán[8], A. Carramiñana[9], S. Casanova[6,10],
O. Chaparro-Amaro[11], U. Cotti[3], J. Cotzomi[12], S. Coutiño de León[13], E. De la Fuente[14], R. Diaz Hernandez[9],
M. A. DuVernois[13], M. Durocher[15], J. C. Díaz-Vélez[14], K. Engel[7], C. Espinoza[1], K. L. Fan[7], N. Fraija[8],
A. Galván-Gámez[8], J. A. García-González[16], F. Garfias[8], M. M. González[8], J. A. Goodman[7], S. Hernandez[1], B. Hona[17],
D. Huang[5], F. Hueyotl-Zahuantitla[2], T. B. Humensky[7], A. Iriarte[8], V. Joshi[18], S. Kaufmann[19], D. Kieda[17], G. J. Kunde[15],
A. Lara[20], H. León Vargas[1], J. T. Linnemann[21], A. L. Longinotti[8], G. Luis-Raya[19], K. Malone[22], O. Martinez[12],
J. Martínez-Castro[11], J. A. Matthews[23], P. Miranda-Romagnoli[24], E. Moreno[12], M. Mostafá[25], A. Nayerhoda[6,26],
L. Nellen[27], R. Noriega-Papaqui[24], E. G. Pérez-Pérez[19], D. Rosa-González[9], E. Ruiz-Velasco[28], H. Salazar[12],
D. Salazar-Gallegos[21], F. Salesa Greus[6,29], A. Sandoval[1], J. Serna-Franco[1], A. J. Smith[7], R. W. Springer[17], O. Tibolla[19],
K. Tollefson[21], I. Torres[30], R. Torres-Escobedo[31], F. Ureña-Mena[9], L. Villaseñor[12], E. Willox[7], H. Zhou[31], C. de León[3],
O. Fornieri[32,33], D. Gaggero[34], D. Grasso[35], A. Marinelli[36,37,38], and S. Ventura[39,40]
HAWC Collaboration
[1] Instituto de Física, Universidad Nacional Autónoma de México, Ciudad de Mexico, México
[2] Universidad Autónoma de Chiapas, Tuxtla Gutiérrez, Chiapas, México
[3] Universidad Michoacana de San Nicolás de Hidalgo, Morelia, Mexico
[4] Department of Physics, St Albert's College (Autonomous), Ernakulam, Cochin, 682018, India
[5] Department of Physics, Michigan Technological University, Houghton, MI, USA
[6] Instytut Fizyki Jądrowej im Henryka Niewodniczanskiego Polskiej Akademii Nauk, IFJ-PAN, Krakow, Poland; amid.nayerhoda@ifj.edu.pl
[7] Department of Physics, University of Maryland, College Park, MD, USA
[8] Instituto de Astronomía, Universidad Nacional Autónoma de México, Ciudad de México, México
[9] Instituto Nacional de Astrofísica, Óptica y Electrónica, Puebla, México
[10] Max-Planck Institute for Nuclear Physics, Heidelberg, Germany
[11] Centro de Investigacíon en Computaci'on, Instituto Politécnico Nacional, México City, México
[12] Facultad de Ciencias Físico Matemáticas, Benemérita Universidad Autónoma de Puebla, Puebla, México
[13] Department of Physics, University of Wisconsin-Madison, Madison, WI, USA
[14] Departamento de Física, Centro Universitario de Ciencias Exactase Ingenierias, Universidad de Guadalajara, Guadalajara, Mexico
[15] Physics Division, Los Alamos National Laboratory, Los Alamos, NM, USA
[16] ITESM, Tecnologico de Monterrey, Escuela de Ingeniería y Ciencias, Ave. Eugenio Garza Sada 2501, Monterrey, NL 64849, Mexico
[17] Department of Physics and Astronomy, University of Utah, Salt Lake City, UT, USA
[18] Erlangen Centre for Astroparticle Physics, Friedrich-Alexander-Universität Erlangen-Nürnberg, Erlangen, Germany
[19] Universidad Politécnica de Pachuca, Pachuca, Hgo, Mexico
[20] Instituto de Geofísica, Universidad Nacional Autónoma de México, Ciudad de Mexico, Mexico
[21] Department of Physics and Astronomy, Michigan State University, East Lansing, MI, USA
[22] Space Science and Applications Group, Los Alamos National Laboratory, Los Alamos, NM, USA
[23] Department of Physics and Astronomy, University of New Mexico, Albuquerque, NM, USA
[24] Universidad Autónoma del Estado de Hidalgo, Pachuca, Mexico
[25] Department of Physics, Pennsylvania State University, University Park, PA, USA
[26] INFN–Sezione di Bari, Via Amendola 173, Bari, I-70126, Italy
[27] Instituto de Ciencias Nucleares, Universidad Nacional Autónoma de Mexico, Ciudad de Mexico, Mexico
[28] Max-Planck Institute for Nuclear Physics, D-69117 Heidelberg, Germany
[29] Instituto de Física Corpuscular, CSIC, Universitat de Valéncia, E-46980, Paterna, Valencia, Spain
[30] Instituto Nacional de Astrofísica, Óptica y Electrónica, Puebla, Mexico
[31] Tsung-Dao Lee Institute and School of Physics and Astronomy, Shanghai Jiao Tong University, Shanghai, People's Republic of China
[32] Gran Sasso Science Institute (GSSI), Viale Francesco Crispi 7, I-67100 L'Aquila, Italy
[33] INFN–Laboratori Nazionali del Gran Sasso (LNGS), Via G. Acitelli 22, I-67100 Assergi (AQ), Italy
[34] INFN–Sezione di Pisa, Largo B. Pontecorvo 3, I-56127 Pisa, Italy
[35] INFN–Sezione di Pisa, Largo B. Pontecorvo 3, Pisa, Italy
[36] Dipartimento di Fisica "Ettore Pancini,"Università degli studi di Napoli "Federico II", Complesso Universitá Monte Sant'Angelo, I-80126 Napoli, Italy
[37] INFN–Sezione di Napoli, Complesso Universitá Monte Sant'Angelo, I-80126 Napoli, Italy
[38] INAF–Osservatorio Astronomico di Capodimonte, Napoli, Italy
[39] Università of Siena, Siena, Italy
[40] INFN, Sezione di Pisa, Pisa, Italy

Abstract

Galactic gamma-ray diffuse emission (GDE) is emitted by cosmic rays (CRs), ultra-relativistic protons, and electrons, interacting with gas and electromagnetic radiation fields in the interstellar medium. Here we present the analysis of teraelectronvolt diffuse emission from a region of the Galactic plane over the range in longitude of

$l \in [43°, 73°]$, using data collected with the High Altitude Water Cherenkov (HAWC) detector. Spectral, longitudinal, and latitudinal distributions of the teraelectronvolt diffuse emission are shown. The radiation spectrum is compatible with the spectrum of the emission arising from a CR population with an *index* similar to that of the observed CRs. When comparing with the DRAGON *base model*, the HAWC GDE flux is higher by about a factor of 2. Unresolved sources such as pulsar wind nebulae and teraelectronvolt halos could explain the excess emission. Finally, deviations of the Galactic CR flux from the locally measured CR flux may additionally explain the difference between the predicted and measured diffuse fluxes.

Unified Astronomy Thesaurus concepts: Gamma-ray astronomy (628); High energy astrophysics (739); Galactic cosmic rays (567); Milky Way disk (1050)

1. Introduction

Cosmic rays (CRs) are highly energetic hadrons and electrons that fill the Galaxy and carry in the solar neighborhood as much energy per unit volume as the average Galactic electromagnetic fields and the thermal and turbulent gas phase, namely, about 1 eV cm^{-3}. CR secondary data suggest that for rigidities around 1 GV cosmic protons and nuclei diffuse in the magnetic fields for a timescale of the order of 10^7 yr before escaping the Galaxy (Berezinskii et al. 1984). At higher energies, CRs are confined for a shorter time in the Galaxy, as evidenced by energy-dependent measurements of the Galactic abundances. The electrically charged nature of CRs does not allow them to travel through space without scattering, absorption, or deflection in the magnetic fields. Thus, these particles redistribute diffusively in the Galaxy contributing to the bulk of Galactic CRs known as background CRs or CR *sea*.

Direct measurements of the spectra of all CR species have recently reached unprecedented quality (Ahn et al. 2010; Adriani et al. 2011, 2019; Aguilar et al. 2015; Yoon et al. 2017). Until a few years ago the CR energy spectrum below petaelectronvolt energies was thought to follow a simple power law (SPL) with a soft index between -2.7 and -2.8. A more complex picture, however, has emerged since PAMELA (Adriani et al. 2011) and AMS (Aguilar et al. 2015) found a hardening (Alemanno et al. 2021) in the spectra of CR proton, helium, and other primary nuclear species at about 300 GeV n^{-1} (GeV per nucleon). Above that energy, a combined fit of PAMELA, AMS, and CREAM (Ahn et al. 2010; Yoon et al. 2017)—the latter probing energies between 1 and 10^3 TeV n^{-1} (n being the atomic mass number)—yields a value very close to -2.6 for the proton spectral index (Lipari 2018). This finding has been confirmed by the CALET experiment, which measured the proton spectrum between 50 GeV and 10 TeV (Adriani et al. 2019). A softening of the spectrum has been recently revealed by DAMPE above a few tens of teraelectronvolts for both proton and helium spectra (An et al. 2019; Alemanno et al. 2021).

Since the direct measurements of CR spectra are necessarily restricted to the proximity of Earth, or for the Voyager measurements (Stone et al. 2013) to the proximity of the solar system, the distribution of CRs in other regions of the Galaxy is not known. It is strongly debated whether the CR sea is homogeneously distributed along the Galactic plane or it shows a gradient toward the inner Galaxy, believed to be produced by a spatial dependence of the transport properties (Evoli et al. 2017, 2008). It is also not clear whether the spectral hardening of the primary CR spectra (at 300 GeV n^{-1}) measured at Earth is representative of the entire CR Galactic population or it is a local effect, originated by the contribution of one or a few nearby CR sources (see, e.g., Thoudam & Horandel 2012). These alternative scenarios can be tested by measuring the diffuse gamma-ray emission from the Galactic plane from gigaelectronvolt to teraelectronvolt energies.

Galactic gamma-ray diffuse emission (GDE) originates from the interactions of the background CRs (hadrons and electrons) with the interstellar medium (ISM) gas and interstellar radiation field (ISRF). CR hadrons interact with matter, producing neutral pions (π^0), which in turn decay into gamma rays, while CR electrons produce high-energy gamma rays via inverse Compton (IC) scattering onto the ISRF photons. At gigaelectronvolt energies, gamma rays are emitted through bremsstrahlung processes when electrons collide with ISM gas.

So far, the diffuse emission of the Galaxy has been primarily investigated in the tens of megaelectronvolts to hundreds of gigaelectronvolts energy range with orbital detectors such as COS-B (Strong et al. 1988), EGRET[41] (Strong & Mattox 1996; Hunter et al. 1997), and the Fermi-Large Area Telescope (LAT).[42] The first analysis of diffuse Galactic emission using Fermi-LAT data generally yielded a good agreement between the local CR spectrum and the CR spectrum in the Galaxy (Ackermann et al. 2012). Recent works (Acero et al. 2016; Yang et al. 2016; Pothast et al. 2018) extract the gamma-ray emissivity in Galactocentric rings and report a hardening and an enhancement of the emissivity in the inner Galactic rings, with a maximum at a distance of $\sim$4 kpc from the Galactic Center.

Measurements of the diffuse emission at teraelectronvolt energies by HEGRA-IACT have determined an upper limit on the ratio of the diffuse photon flux to the hadronic CR flux $<$ 2.0×10^{-3} near the inner Galaxy at 54 TeV (Aharonian et al. 2002). GDE measured with Milagro at a median energy of 15 TeV for Galactic longitudes between 30° and 110° and between 136° and 216° and for Galactic latitudes between $-10°$ and $+10°$ is consistent with the predictions of the GALPROP optimized model everywhere except for the Cygnus region (Abdo et al. 2008). Measurements of the diffuse emission at teraelectronvolt energies by the ARGO-YBJ detector have yielded a soft gamma-ray spectrum with an index of -2.9 ± 0.3 within the region $40° < l < 100°$ and $|b| < 5°$ in Galactic longitude and latitude, respectively (Bartoli et al. 2015). Measurements with the H. E. S. S. instrument favor a significant contribution of $\pi0$ decay to the total signal of the diffuse emission at teraelectronvolt energies from the Galactic plane (Abramowski et al. 2014). A recent study of the diffuse radiation from the Galaxy at 100 TeV by the Tibet AS-Gamma Collaboration shows that CRs are accelerated beyond petaelectronvolt energies in our Galaxy and spread over the Galactic disk. The hadronic diffuse component is likely the dominant component of this sub-petaelectronvolt emission (Amenomori

---

[41] https://heasarc.gsfc.nasa.gov/docs/cgro/egret/
[42] https://fermi.gsfc.nasa.gov/

Table 1
Properties of the Nine Analysis Bins

	Properties of the Analysis Bins		
$\mathcal{B}$	f_{hit} (%)	ψ_{68} (deg)	$\tilde{E}_\gamma^{\text{MC}}$ (TeV)
1	6.7–10.5	1.03	0.7
2	10.5–16.2	0.69	1.1
3	16.2–24.7	0.50	1.8
4	24.7–35.6	0.39	3.5
5	35.6–48.5	0.30	5.6
6	48.5–61.8	0.28	12
7	61.8–74.0	0.22	15
8	74.0–84.0	0.20	21
9	84.0–100.0	0.17	51

Note. Bin number: $\mathcal{B}$, event size: f_{hit}, 68% PSF containment: ψ_{68}, and median energy for a reference source of spectral index: -2.63 at a decl. of 20° $\tilde{E}_\gamma^{\text{MC}}$ (Abeysekara et al. 2017a).

et al. 2021). Very recently petaelectronvolt diffuse radiation has been detected by LHAASO (Cao et al. 2023).

The High Altitude Water Cherenkov (HAWC) Gamma-Ray Observatory,[43] located in Mexico, is well-designed to study CRs and gamma rays at energies between 300 GeV and above 100 TeV. The detector observes the Cherenkov lights in the water produced by the charged secondary particles. Thanks to its large field of view, it monitors two-thirds of the sky daily with a >95% duty cycle (Abeysekara et al. 2017b, 2023).

Here we present the analysis of the HAWC data above 300 GeV and up to 100 TeV within the region of interest (ROI) spanning $l \in [43°, 73°]$ in longitude and $b \in [-5°, 5°]$ in latitude (see Section 3). The spectra and profiles of the GDE are measured and shown within specific portions of the Galactic plane included in ROI (namely, $b \in [-2°, 2°]$, $b \in [-4°, 4°]$, and $b \in [-5°, 5°]$). Future analysis will extend the range in longitude to cover the entire part of the sky visible to HAWC. Finally, we compare the measured GDE spectra as well as its latitudinal and longitudinal profiles with those obtained with a reference CR transport model implemented with the DRAGON code (Evoli et al. 2008, 2017).

This paper is organized as follows. The analysis of the diffuse emission from the Galactic plane is described in detail in Section 2. Section 3 presents a discussion and a comparison of the HAWC results with other measurements. Section 4 presents our conclusions. The differential flux profiles are presented in Appendix A, and the comparative analysis between ARGO-YBJ measurements and DRAGON prediction is delineated in Appendix B. The DRAGON code is also introduced in Appendix C.

2. Analysis

2.1. Data Set

The analysis presented in this study is based on a data set accumulated over 1347 days by HAWC from 2015–2019. Standard reconstructed data generated by the HAWC production of Pass 4 (Abeysekara et al. 2017a) is used. The data are categorized into nine energy bins corresponding to the fraction f_{hit} (fractional hit) of PMTs triggered based on the sum of the active PMTs (Abeysekara et al. 2017b). In Table 1, the $\tilde{E}_\gamma^{\text{MC}}$

column represents the median energy of the simulated gamma-ray photons in the different analysis bins for a Crab Nebula–like source (decl. = 20° and for an energy spectrum $E^{-2.63}$). By choosing bins 1–9 in the analysis, an energy range between 300 GeV to more than 100 TeV (Abeysekara et al. 2017a) is considered.

2.2. Analysis Regions

The analysis of the diffuse emission reported here is focused on an ROI restricted to a portion of the Galactic plane within the intervals $l \in [43°, 73°]$ in longitude and $b \in [-5°, 5°]$ in latitude, as defined in the Galactic coordinate system. The analysis is carried out by dividing the longitudinal range of the ROI into three subregions, namely, $l \in [43°, 56°]$, $l \in [56°, 64°]$, and $l \in [64°, 73°]$, each region being defined in such a way that no significance excess larger than five ($\sigma > 5$) is located on the borders of the regions. Hence, none of the regions shares a source.

2.3. Event and Background Maps

In HAWC the data analysis is based on the production of maps of the events and background. The background is estimated with a method known as *direct integration*, which is used to fit the isotropic distribution of events that pass the gamma-ray event selection (Atkins et al. 2003). The event maps are simple histograms of the reconstructed events $\lambda_{ij} = b_{ij} + \sum_k \gamma_{ijk}$, that pass gamma/hadron cuts (Abeysekara et al. 2017a), where λ_{ij} is the event count in the jth pixel of the ith f_{hit} bin, b_{ij} is the background events in the jth pixel of the ith f_{hit} bin, and γ_{ijk} is the expected number of gamma rays from the kth source in the jth pixel of the ith f_{hit} bin (data = background + signal).

For the present analysis, the maps are produced using HEALPix pixelization (Hanisch et al. 2001). The map pixelization is performed with Nside = 1024 for a mean spacing between pixel centers of about 0°.05, which is small compared to the typical point-spread function (PSF) of the reconstructed events as shown in Table 1 (the ψ_{68} column represents the 68% containment angle of the PSF, for a source similar to the Crab Nebula).

In Figure 1, the significance map[44] of the data measured by HAWC from the Galactic plane (hereafter called the *original map*) is shown, and the corresponding 1D significance histogram is presented in Figure 2. We do not show the maps beyond $b \in [-4°, 4°]$ as the radiation is not significant at higher latitudes.

2.4. Analysis of the GDE

The radiation measured by HAWC from the Galactic plane, shown in Figure 1 (original map), is the sum of different contributions: GDE, produced by background CR protons and electrons, and emission from pointlike and extended gamma-ray sources. The total flux measured by HAWC from the Galactic plane, F_{tot}, can thus be written as

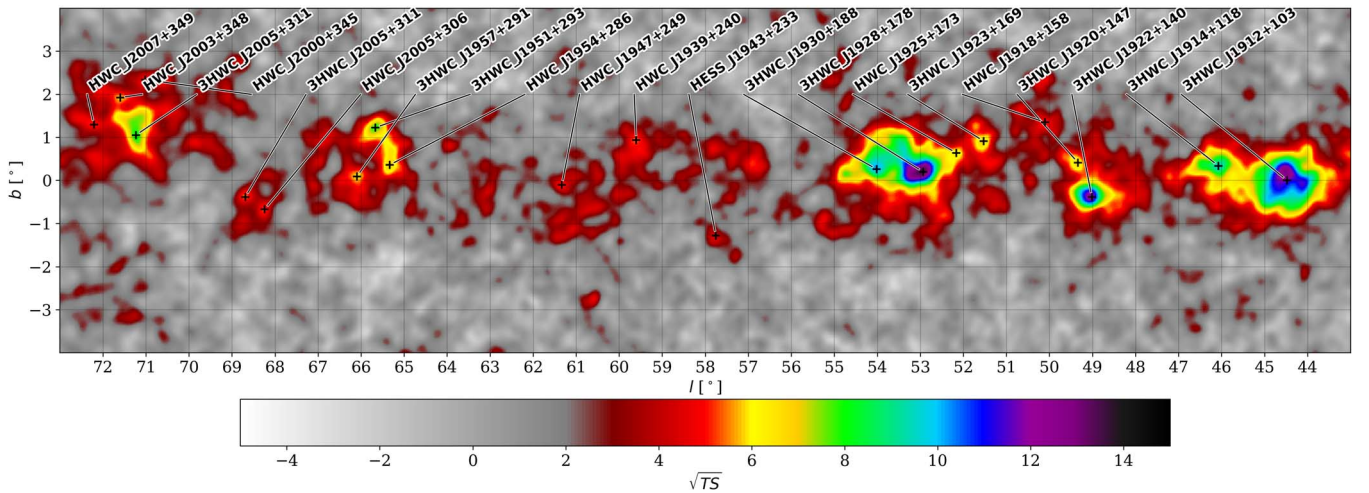$$F_{\text{tot}} = F_{\text{sources}} + F_{\text{GDE}}, \qquad (1)$$

Figure 1. Significance map of the total emission measured by HAWC (original map) shown over a range in latitude between $b \in [-4°, 4°]$. A significance map is a 2D visualization of the significance value per each pixel, where significance $= \sqrt{TS}$ (Wilks 1938), and TS is the test statistic, as defined using the likelihood ratio (Abeysekara et al. 2017a).

where $F_{sources}$ is the flux produced by all sources ($\Sigma_i F_{source_i}$), and F_{GDE} is the flux corresponding to the GDE. The original map is the starting point of the analysis of the GDE, which will essentially be carried out in two steps. In the first step, a map of the source emission will be obtained and then subtracted from the measured HAWC map (original map, Figure 1). In this way, a *source-subtracted* map, which in principle should contain only GDE radiation, will be generated. In the second step, the analysis of the source-subtracted map will yield the spectral, longitudinal, and latitudinal features of the GDE emission.

The contribution of source emission to the total emission is obtained by a multiple-source fitting process, in which a model for the total radiation, including pointlike or extended gamma-ray sources resolved by HAWC and the GDE (treated as an extended source), is fitted to the original map.

The best fit for the hotspots—characterized as significance excess larger than three ($\sigma > 3$)—in the original map, results in 21 (either pointlike or extended) sources, as labeled in Figure 3.[45]

The present study proposes a model in which the spectral distributions of the 21 sources are assumed to follow power-law spectra with exponential cutoffs, while the spectral distribution for the diffuse emission is represented by an SPL. Furthermore, the morphological shape of extended sources in the model is approximated by a Gaussian distribution. To incorporate the morphological features of the GDE, a two-dimensional morphological template is included in the model, which is obtained by summing the contributions of $\pi0$ decay and IC from the DRAGON code (see Appendix C).

The spectral parameters of both the GDE and the sources, as well as the size of extended sources, are considered as free parameters allowed to vary and be fitted. The fitting procedure is performed using a likelihood method based on the Multi-Mission Maximum Likelihood (3ML) framework (Vianello et al. 2015). The objective is to identify the best-fitting model

that characterizes the spectral and morphological properties of all 21 sources in the Galactic plane. To assess the optimal model, a residual map and significance histogram are obtained by subtracting the model for sources and GDE (Figure 3, bottom) from the original map. This procedure is repeated many times until the optimal model, for which the residual map shows no significant additional hotspots is obtained. The residual or background map is shown in Figure 4.

The multisource fitting thus yields the best possible fit for the spectrum and morphology of all sources, and therefore, the total flux due to all sources ($F_{sources}$). Figure 3 (top) shows the map of the fitted source flux. The GDE reference model used in the fitting procedure is plotted in the middle panel, while the model of GDE + sources is shown in the bottom panel.

In Figure 5, the significance histogram of the residual map in the region restricted to $b \in [-2°, 2°]$ and to $b \in [-4°, 4°]$ is presented. The residual map, which shows no excess above 5σ, helps test the goodness of the models assumed for sources and GDE.

We subtract the model of the sources in Figure 3 (top) from the original map (Figure 1) to obtain a *source-subtracted map* (GDE map) shown in Figure 6, ($F_{GDE} = F_{tot} - F_{sources}$), which is used to determine the GDE spectral properties in the final step of the analysis.

3. Results

3.1. Galactic Diffuse Emission Spectrum

The GDE distribution is reported in Table 2 for the regions of the Galactic plane over latitude ranges of $|b| < 2°$ and $|b| < 4°$. The contribution of the GDE flux with respect to the total flux measured with HAWC is computed for two energy ranges and reported as f_{10} and f_{100}.[46] f_{10} is the fractional contribution of the GDE flux to the total flux for energies between 300 GeV and 10 TeV, while f_{100} is the fractional contribution of the GDE flux to the total flux up to 100 TeV.

As shown in Table 2 the contribution of the GDE flux (both f_{10} and f_{100}) varies between 67.2% and 88.1%, which implies

---

[45] Spectral parameters and extension (in the case of extended sources) of sources labeled in significance maps differ from those in the catalogs (H. E. S. S. Abdalla et al. 2018), HAWC Albert et al. 2020), since they are based on a model fitting including a GDE model in the analysis.

[46] $f_x = \frac{\int_{0.3(TeV)}^{x} F_{GDE}}{\int_{0.3(TeV)}^{x} F_{tot}}$, where F_{GDE} and F_{tot} are GDE flux and total HAWC flux respectively.
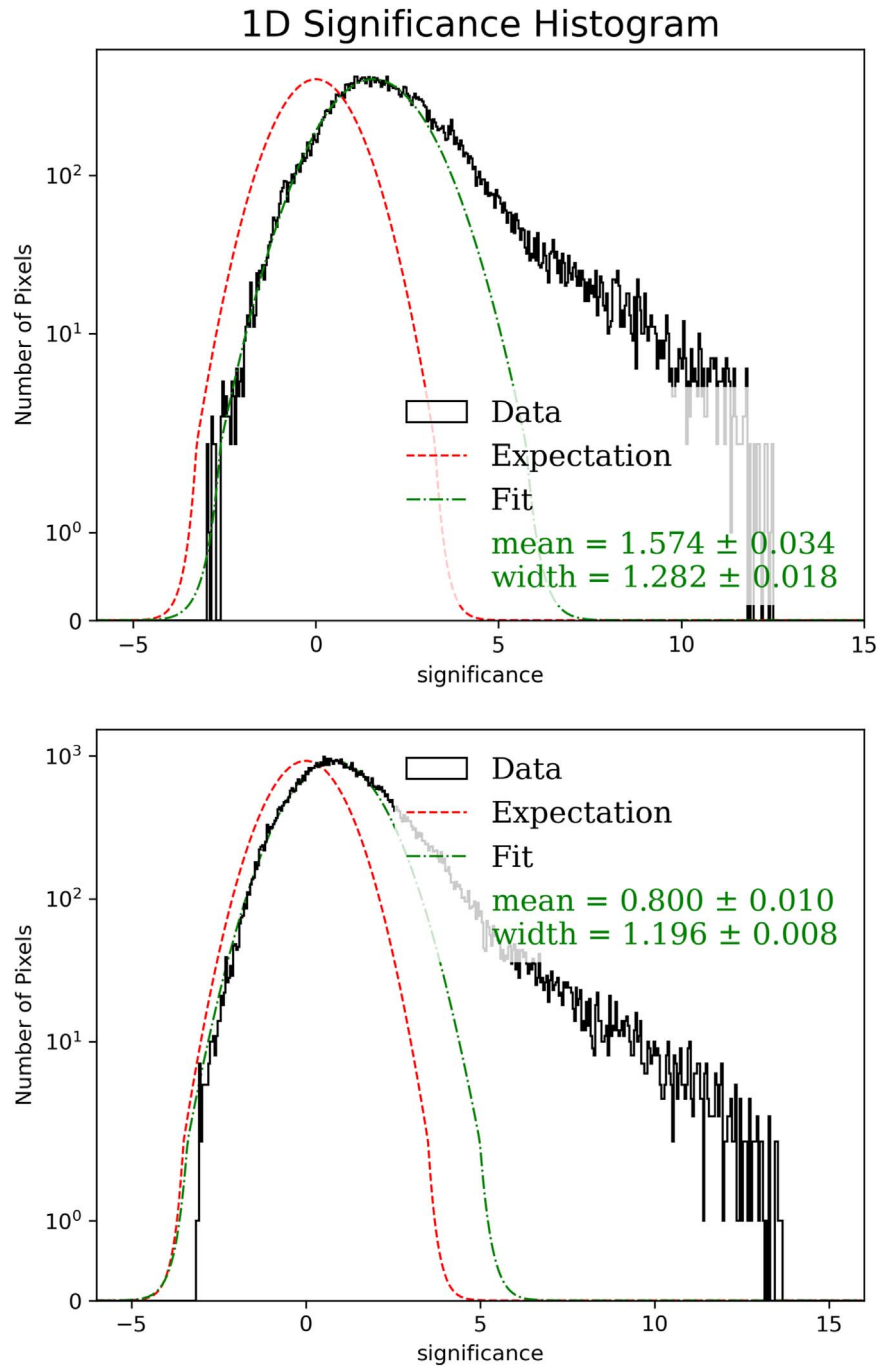
1D Significance Histogram

Figure 2. Significance histograms of HAWC data in the region restricted in $l \in [43°, 73°]$ and $b \in [-2°, 2°]$ (top) and in $l \in [43°, 73°]$ and $b \in [-4°, 4°]$ (bottom). The red-dashed line represents a standard normal distribution and the green line represents a Gaussian fit of the significance of the given data. There is an excess with a significance greater than ∼5 in the region considered.

that the GDE contributes significantly to the total emission of teraelectronvolt gamma rays from the Galactic plane. The average GDE flux (per sr) over latitudes $|b| < 2°$ is greater than the average GDE flux in the broader regions with $|b| < 4°$. In the regions closer to the center of the Galactic disk ($b = 0$), the GDE is in fact expected to be brighter (see Figure 8). On the other hand, both fractional contributions, f_{10} and f_{100}, show that the GDE is less dominant for $|b| < 2°$ (see Table 2). In the outer Galaxy, the emission from identified sources contributes less, as expected.

The average spectral index over the region $43° < l < 73°$ varies from -2.61 ± 0.03 for latitudes $|b| < 2°$ to -2.60 ± 0.03 $|b| < 4°$. Assuming that the GDE is mostly contributed by

hadronic interactions, from the spectral feature of the GDE, we can deduce the spectral feature of the CR population producing this emission. The spectral index of the Galactic background CR population over an energy range between 1 and 10^3 TeV, which has a value very close to -2.6, well agrees with the results obtained by Lipari (2018). On the other hand, our result disagrees with previous studies of the CR spectrum below petaelectronvolt energies that assumed the spectrum to follow an SPL with a soft index between -2.7 and -2.8 (Abdo et al. 2008). While the contribution of unresolved sources to the GDE and its relevant effect on the average spectral index should be taken into account (a further discussion on this is given in
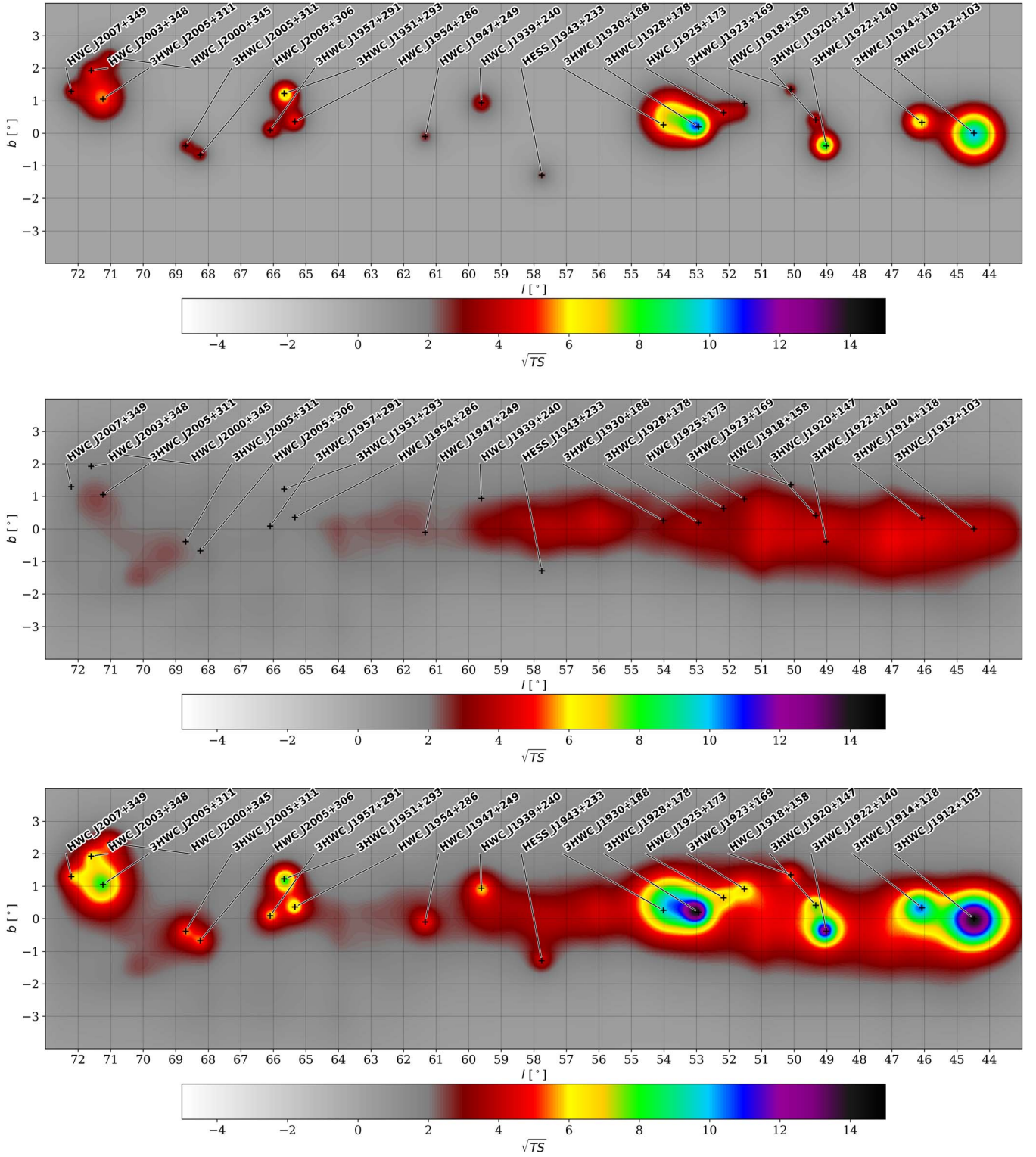
Figure 3. Significance maps of the reference models. Top: the fitted model for pointlike and extended sources used to obtain the source-subtracted map. Middle: reference model of GDE obtained from DRAGON. Bottom: sum of the fitted model for the sources and GDE.

Section 4), yet the spectral index of the GDE measured with HAWC reveals that the CR population producing GDE along the Galactic plane has (on average) a spectral index compatible with the spectral index of the locally measured CR population up to tens of teraelectronvolts (see Section 1). The harder spectral indices of the GDE of some subregions (as shown in Table 2) are likely due to the contribution of unresolved sources.

3.2. Profile Generation

Galactic longitudinal and latitudinal profiles provide valuable information on the distribution of the GDE along the Galactic plane.

The longitudinal profile is created by averaging the energy flux (see Equation (2)) within 10 bins, each defined in a 3° longitudinal range, over a latitude range of $|b| < 2°$. The
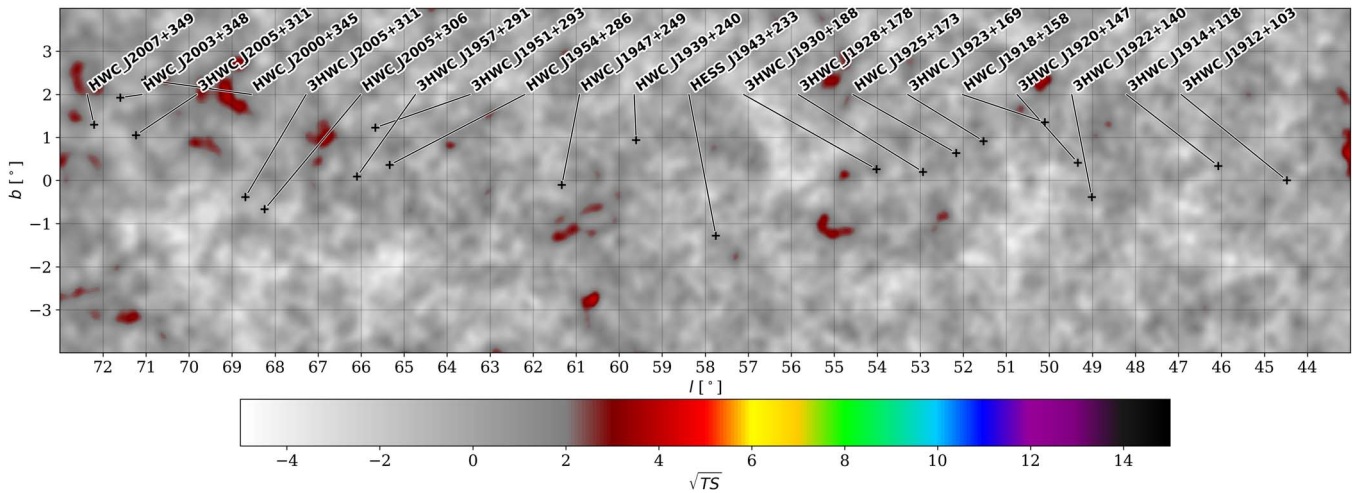
Figure 4. Significance of the residual map, created by subtracting the model of the source and GDE (Figure 3, bottom), obtained in the multisource fitting procedure, from the original map (Figure 1).

resulting bins collectively span the entire longitudinal range of analysis, covering 30° in total. Conversely, the latitudinal profile is generated by averaging the energy flux over the entire longitude range within nine bins, each defined in a 1° latitudinal range. This approach enabled us to cover the latitude range of $|b| < 4°.5$.

The energy flux (Equation (2)) is computed over the energy range between 300 GeV (E_{min}) and 100 TeV[47] (E_{max}),

$$F(E_{min}, E_{max}) = \int_{E_{min}}^{E_{max}} E\phi(E)dE$$

$$= \phi_0 \frac{E_0^2}{-\Gamma + 2}\left(\frac{E}{E_0}\right)^{-\Gamma + 2} \Bigg|_{E_{min}}^{E_{max}}, \qquad (2)$$

where $\phi(E) = \phi_0(E/E_0)^{-\Gamma}$, as E_0 is a reference energy, ϕ_0 is the differential flux at E_0 and Γ is the spectral index.

Profiles are computed for both the original map (Figure 1) and the GDE map (Figure 6); therefore, it is possible to compare the level of the energy flux of the total flux measured by HAWC, F_{tot}, (red line) with those parameters of the diffuse emission (blue line) along the Galactic plane.

In the profiles, vertical error bars represent the statistical error, and horizontal error bars show the width of each bin in which the GDE parameters are calculated in. The brown lines in longitudinal profiles indicate the subregions as explained in Table 2.

In the longitudinal profiles in the range between $56° < l < 64°$ (Figure 7), no bright sources were identified in our analysis; the difference between the GDE and the total emission (represented by the blue and red lines, respectively) reaches a minimum value. The f_{100} is 88.1% (see Table 2) and the spectrum of the total emission is similar to the GDE spectrum.

Figure 8 represents the latitude profile of the total energy flux measured by HAWC (red), GDE flux (blue), and DRAGON estimation for the π0 decay, and IC production mechanisms. The error bars increase on the edge of the latitude profiles due to the lack of statistics in these regions.

---

47 In Table 2, the energy flux is also computed up to 10 TeV.

3.3. Comparison with Other Observations of the GDE

Observations of teraelectronvolt GDE, performed by different experiments such as Milagro (Abdo et al. 2008), LHAASO-KM2A (Cao et al. 2023), HEGRA-IACT (Aharonian et al. 2001), and ARGO-YBJ (Bartoli et al. 2015) are shown in Figure 9. The Milagro points for longitudes $30° < l < 65°$ and $65° < l < 85°$ are obtained at 15 TeV (Abdo et al. 2008) energies. An upper limit was set by HEGRA-IACT at 1 TeV with a 99% confidence level (C.L.; Aharonian et al. 2001).

When compared with the results obtained with Milagro, the findings of this study reveal a smaller level of the GDE as measured by HAWC data. This disparity can be attributed to the utilization of a model (see Section 2.4) that more effectively accounts for source emissions, leading to a better fit of the data and improved estimation of the true level of GDE. As a consequence, the HAWC study reaches a lower threshold for the *true* GDE compared to the previous work by Milagro. LHAASO reported the energy spectrum of the GDE within the energy range of 10 TeV to 1 PeV. The observed spectrum, found in the inner region ($15° < l < 125°$, $|b| < 5°$), follows a power-law function with an index of -2.99 ± 0.04.

HEGRA-IACT (Figure 9) reported an upper limit for GDE above 1 TeV (99% C.L.) with a presumed spectral index of -2.6 (Aharonian et al. 2001). As shown in Figure 9, the HAWC measurement is below HEGRA's upper limit; this excess suggests a significant contribution of unresolved sources in GDE measured by HEGRA-IACT, likely due to the nonideal modeling for the sources in the HEGRA-IACT analysis. Moreover, HEGRA-IACT has measured the GDE in a narrow region closer to the Galactic Center (lower Galactic longitude), which is expected to have a more significant diffuse emission (as can be seen in Figure 6). In Figure 9, the estimated spectra of DRAGON for the π0-decay mechanism, and total diffuse emission (which is a sum of the π0 decay and IC) are shown. The IC contribution modeled with DRAGON is negligible. In Figure 9 we also include a comparison with the ARGO-YBJ measurements. However, we remark that a comparison of HAWC findings with the ARGO-YBJ results is difficult. ARGO-YBJ reported the GDE emission from higher longitudes (further away from the Galactic Center), with energies ranging from ∼350 GeV to ∼2 TeV.
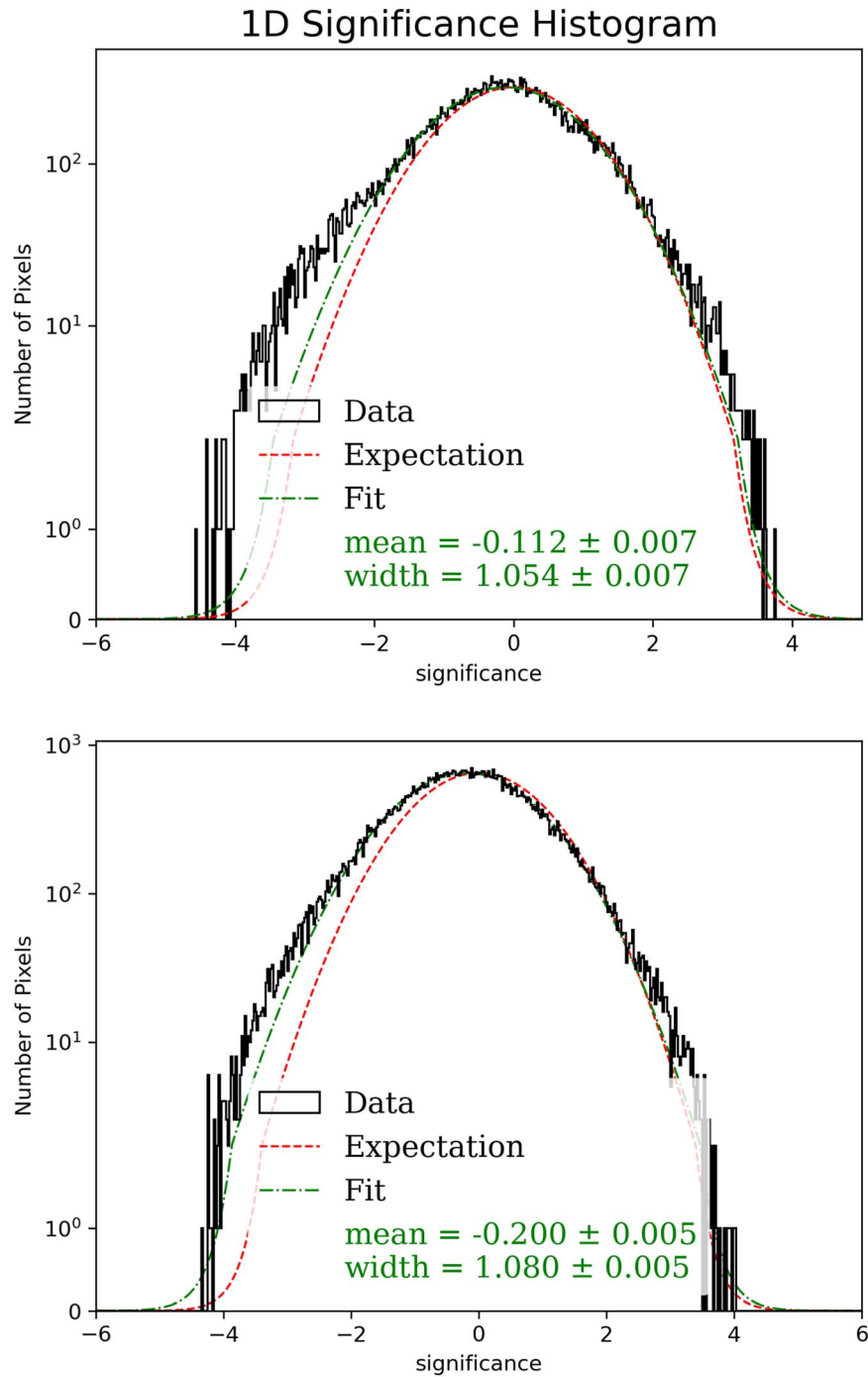
1D Significance Histogram

Figure 5. Significance histograms of the residual map in the region restricted in $l \in [43°, 73°]$ and $b \in [-2°, 2°]$ (top) and in $l \in [43°, 73°]$ and $b \in [-4°, 4°]$ (bottom). The red-dashed line represents a standard normal distribution and the green line represents a fit of the significance of the given data.

4. Discussion and Conclusion

We have presented the first analysis of the spectral and angular distribution of the GDE measured by HAWC above 1 TeV over a portion of the Galactic plane between a longitude and latitude of $l \in [43°, 73°]$ and $b \in [-5°, 5°]$, respectively. We have determined both the longitudinal and latitudinal profiles of this emission and its spectrum in several subregions.

We have found that the spectrum of the emission is well fitted by an SPL model with an index of -2.61 ± 0.03 (see Table 2). Such a spectral index well agrees with the emission being generated by a population of background CR protons and

heavier nuclei, whose spectral shape very closely mimics the spectral shape of the CR spectrum probed by experiments near Earth (see Section 1). Our results support the picture in which the CR spectral hardening found by PAMELA and AMS at the rigidity of about 300 GV is a large-scale feature as also suggested by the AMS measurements of secondary CR nuclei spectra (Aguilar et al. 2018).

In this study, we compared the predictions of a reference model, known as the *base model*, implemented using the DRAGON code, with the measured spectral shape of the GDE in the sky window observed by the HAWC. The base DRAGON model solves CR propagation in the Galaxy assuming standard
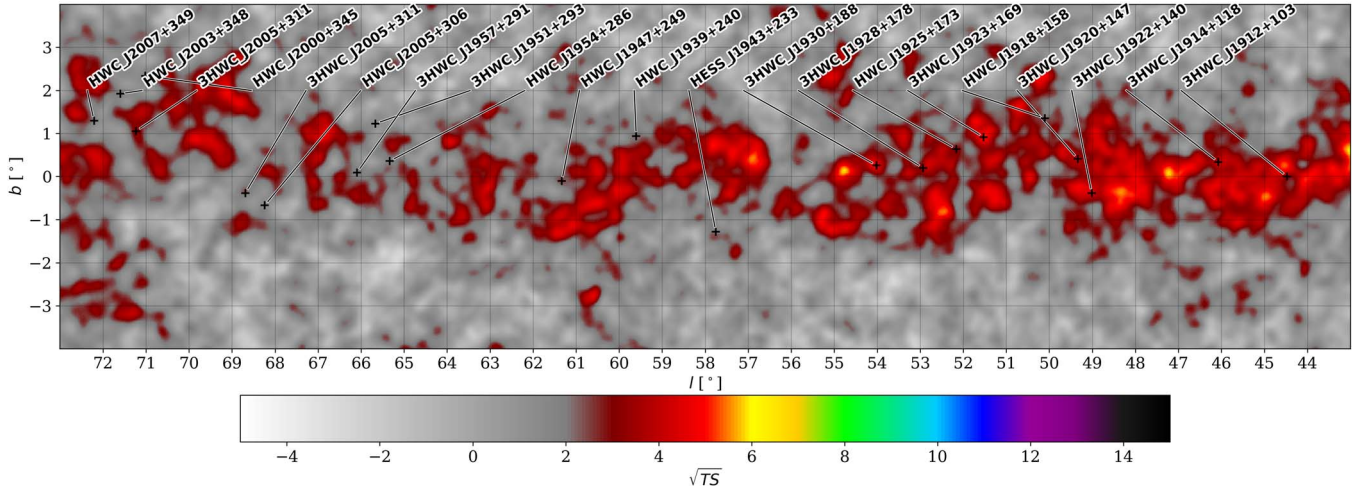
Figure 6. Significance map of the source-subtracted map, generated by subtracting the model of the source (Figure 3, top), obtained in the multisource fitting procedure, from the original map (Figure 1).

Table 2
Spectrum of the GDE in Various Subregions of the ROI

l_{min} (deg)	l_{max} (deg)	$|b| <$ (deg)	$F_7 \times 10^{-12}$ (TeV^{-1} s^{-1} cm^{-2} sr^{-1})	Index	f_{10} (%)	f_{100} (%)
43	73	2	$8.89 \pm 0.37^{-0.70}_{+0.48}$	$-2.61 \pm 0.03^{-0.04}_{+0.02}$	72.7	71.8
43	73	4	$5.45 \pm 0.25^{-0.44}_{+0.38}$	$-2.60 \pm 0.03^{-0.04}_{+0.01}$	76.1	75.3
43	56	2	9.9 ± 0.6	-2.70 ± 0.04	68.8	67.4
43	56	4	5.8 ± 0.4	-2.69 ± 0.05	73.1	71.7
56	64	2	8.9 ± 0.7	-2.58 ± 0.06	86.4	86.6
56	64	4	5.2 ± 0.5	-2.60 ± 0.07	87.9	88.1
64	73	2	7.8 ± 0.7	-2.48 ± 0.07	67.2	67.2
64	73	4	5.5 ± 0.45	-2.51 ± 0.06	73.7	73.4

Note. The first error represents the statistical error; the second shows the systematic uncertainty. For each region, the GDE parameters are reported for $|b| < 2°$ and $|b| < 4°$. f_{10} and f_{100} are the fraction of the GDE flux with respect to the total flux, up to 10 TeV and 100 TeV respectively. The flux F_7: differential flux at 7 TeV. The same sources of systematic uncertainty considered in HAWC's performance papers (Abeysekara et al. 2017c, 2019) are considered here.

CR transport properties, namely, a CR diffusion coefficient as obtained from measurements of secondary CR ratios. The CR spectra over the whole Galaxy are then convolved with the gas distribution. The spectral properties of the DRAGON base model agreed well with the GDE measurements. The model underpredicted the GDE measured by HAWC by a factor of ~2, averaged over the entire region (see Figure 9).

This discrepancy may be attributed to a variety of factors, including potential underestimation of the density of CRs or gas, as well as uncertainties related to their respective distributions, particularly in the case of CRs, which are still largely unknown. In addition, the contribution from unresolved sources cannot be overlooked, as it has been shown that up to 90% of the diffuse radiation at teraelectronvolt energies can originate from such sources (Cataldo et al. 2020; Steppa & Egberts 2020). Another limitation that cannot be ignored is the nonideal model for sources used in this study, which causes the GDE to include emission from sources left in the source-subtracted map. Furthermore, the teraelectronvolt halos of pulsar wind PWNe are also expected to make a significant contribution to the emission at both gigaelectronvolt and teraelectronvolt energies (Vecchiotti et al. 2022). In this sense, our measurement of the GDE can be seen as an upper limit to the *truly* diffuse emission. Also, it should be kept in mind that systematic errors (angular and energy resolution) restrict the analysis precision (Abeysekara et al. 2017b).

Future HAWC analyses using higher-quality data, such as Pass 5 data, will be necessary to further elucidate the difference between the measured and predicted diffuse fluxes. Very recently LHAASO published a measurement of the diffuse emission from a large region of the Galactic plane, $15° < l < 125°$ and $-5° < b < 5°$, by excluding large portions of the Galactic plane, and reported a significantly lower level for the diffuse emission with respect to HAWC (Cao et al. 2023). The analysis of teraelectronvolt diffuse emission will be a major scientific objective for future gamma-ray observatories, such as the SWGO observatory (Huentemeyer et al. 2019) and the Cherenkov Telescope Array (The Cherenkov Telescope Array Consortium et al. 2017), which will benefit from improved sensitivity and angular resolution.
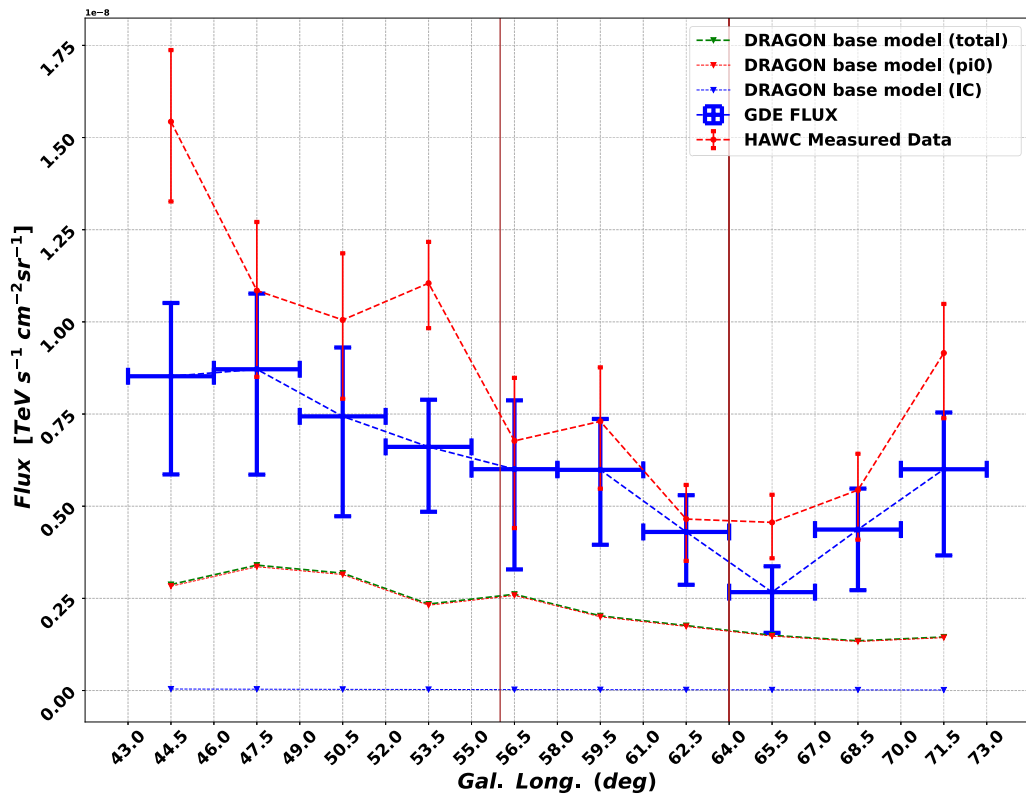
Figure 7. Longitude profiles for energy flux between 300 GeV and 100 TeV, the red line refers to the total flux (F_{tot}), the blue line represents the GDE, as well as the prediction of diffuse emission by DRAGON for the $\pi 0$ decay and IC production mechanism. The brown lines show the border of the regions as explained in Table 2.
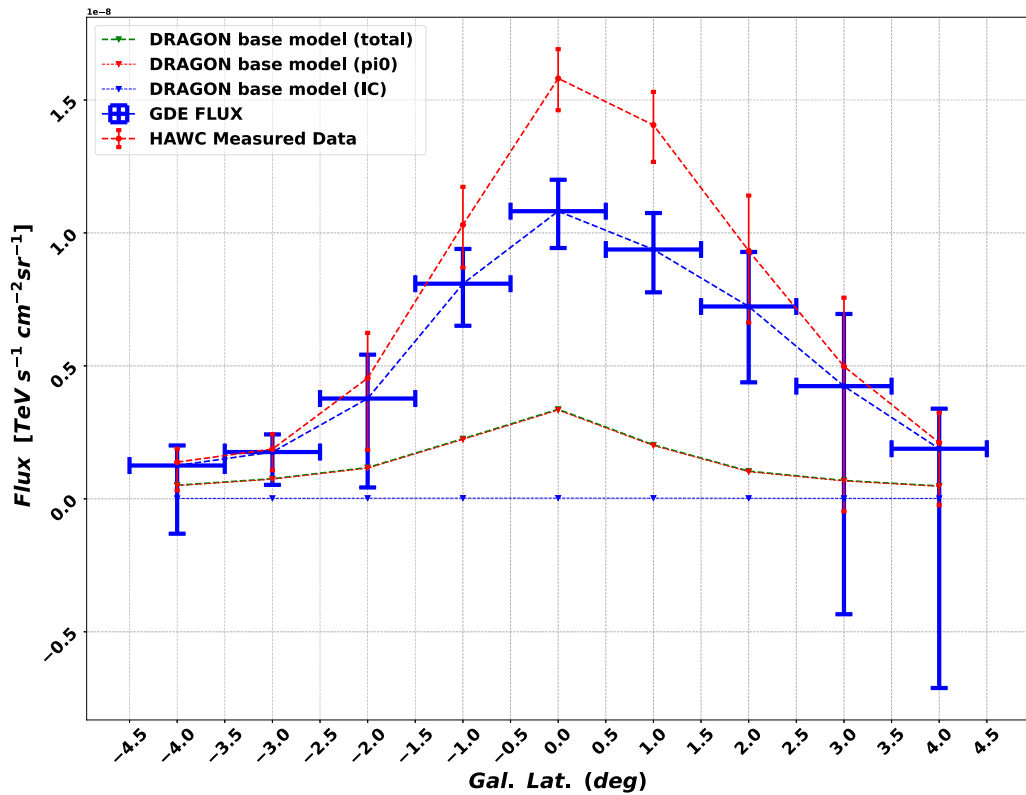

Figure 8. Latitudinal profile for the energy flux between 300 GeV and 100 TeV, red and blue lines refer to the total flux measured by HAWC and the GDE, respectively. DRAGON estimation for the $\pi 0$ decay and IC production mechanism are also presented.
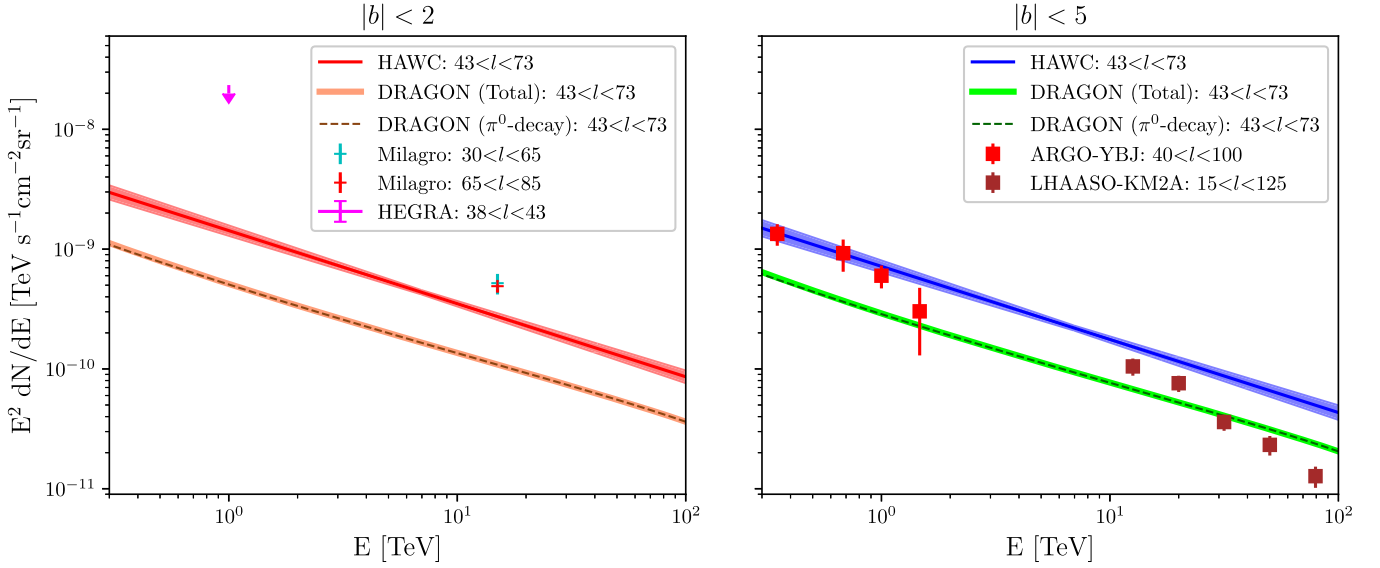
Figure 9. Spectra of the GDE measured by different experiments at different regions, and DRAGON estimations for total and π^0-decay emission; HAWC and DRAGON within $43° < l < 73°$ (left panel: $|b| < 2°$, and right panel: $|b| < 5°$), statistical errors and the systematic errors are listed in Table 2. Milagro at 15 TeV for two regions within $|b| < 2°$ (Abdo et al. 2008). An upper limit quoted by HEGRA-IACT (99% C.L.) in $|b| < 2°$ (Aharonian et al. 2001). ARGO-YBJ in $40° < l < 100°$ (Bartoli et al. 2015), and LHAASO-KM2A in $15° < l < 125°$ (Cao et al. 2023), both within $|b| < 5°$.

Appendix A
Differential Flux Profiles

As previously discussed in Section 3.2, longitudinal and latitudinal profiles are used to study the distribution of GDE along the Galactic plane. This appendix presents the longitudinal and latitudinal profiles for the differential flux of the GDE emission at $E_0 = 7$ TeV. The longitudinal profile is obtained by averaging the differential flux over a range in

latitude of $|b| < 2°$. The latitudinal profile is obtained by averaging the differential flux over a range in longitude of $l \in [43°, 73°]$, which covers the latitude range of $|b| < 4°.5$.

The longitudinal profile of the differential flux (Figure 10), as discussed in Section 3.2, exhibits a minimum difference between the GDE and total emission, represented by the blue and red lines, respectively, in the range of $56° < l < 64°$. In addition, Figure 11 shows the latitudinal profile of the
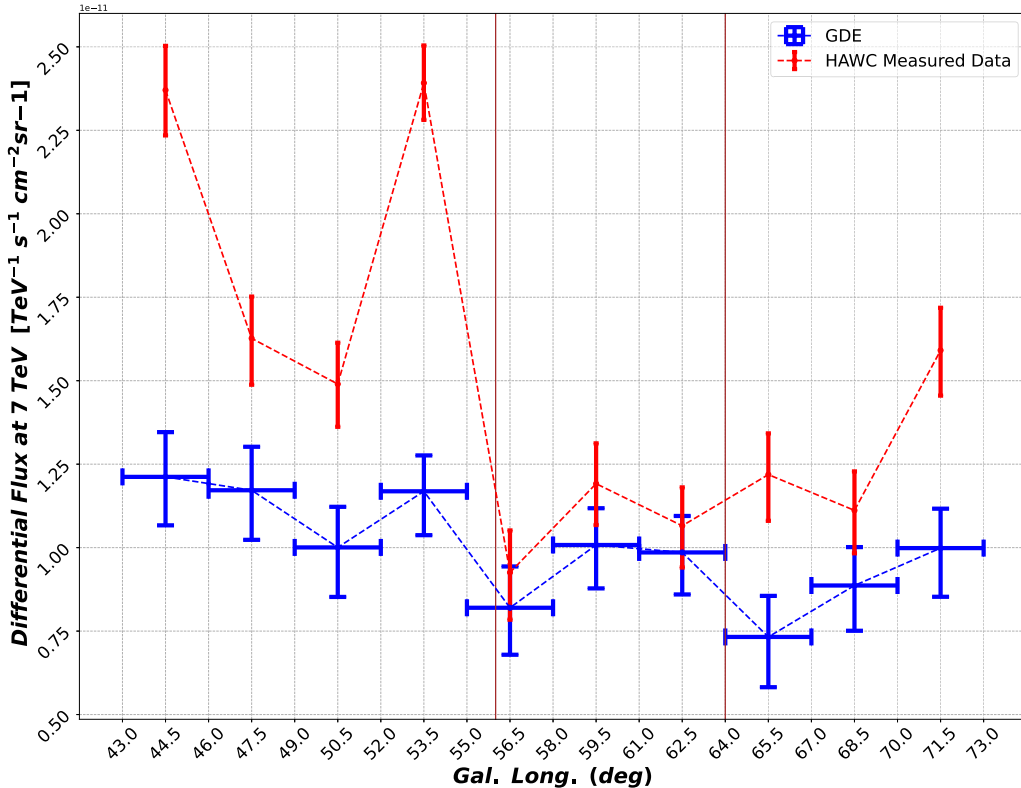

Figure 10. Longitudinal profile of the differential flux (at 7 TeV); the blue line represents the GDE differential flux with an error bar, while the red line shows the longitudinal profile of the total flux (F_{tot}) measured by HAWC. The vertical brown lines are borders of subregions.
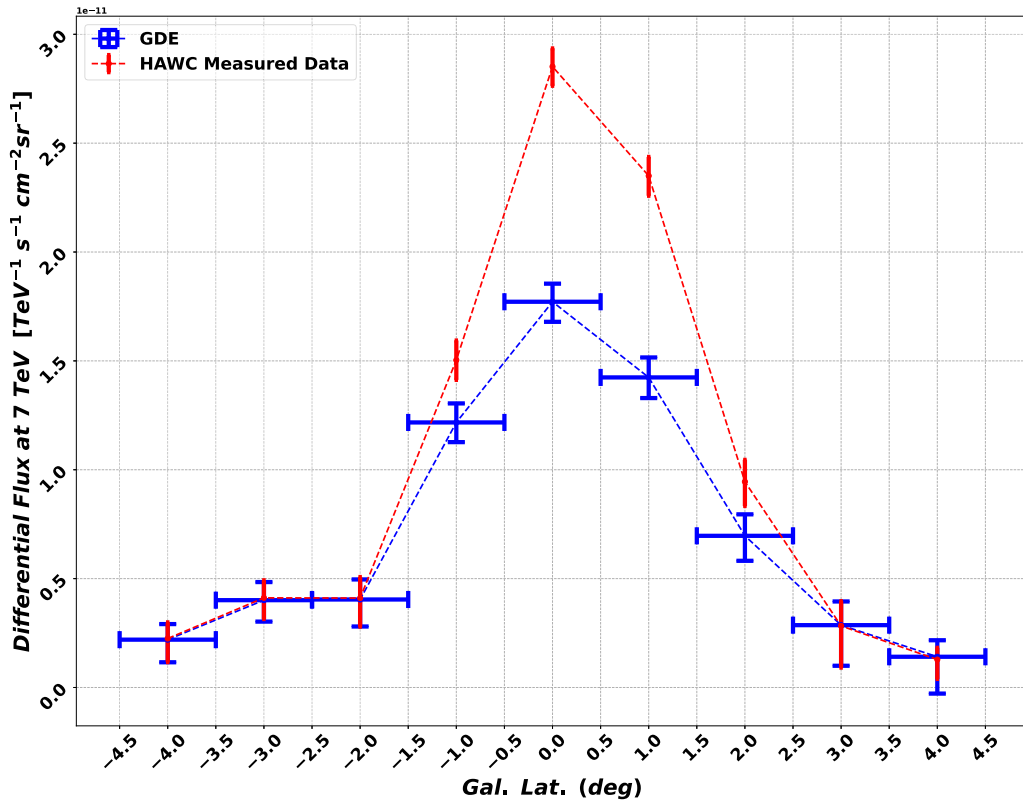
Figure 11. Latitudinal profile of the differential flux (at 7 TeV). The differential flux of the diffuse emission is represented by blue lines with error bars, while the red line refers to the total differential flux measured by HAWC.

differential flux of the GDE and the total emission measured by HAWC (within the same bins).

Appendix B
Comparison with ARGO-YBJ Measurements

The measurement of the diffuse emission by ARGO-YBJ (Bartoli et al. 2015) at Galactic longitudes of $40° < l < 100°$ and Galactic latitudes of $|b| < 5°$ and for an energy range from $\sim$350 GeV to $\sim$2 TeV is shown in Figure 12. The measured flux

at three median energies, 350 GeV, 680 GeV, and 1.47 TeV (with uncertainties of about 30%) is above the DRAGON estimations of GDE. Additional flux from unresolved sources and from PWNe halos might explain the discrepancy between the ARGO-YBJ results and the DRAGON predictions. The spectral index of the GDE as measured by ARGO-YBJ is -2.9 ± 0.31, which is softer than the HAWC spectral index. For comparison, we show also the HAWC flux measured in $43° < l < 73°$ and Galactic latitudes of $|b| < 5°$, which is however measured from an inner region of the Galactic plane.

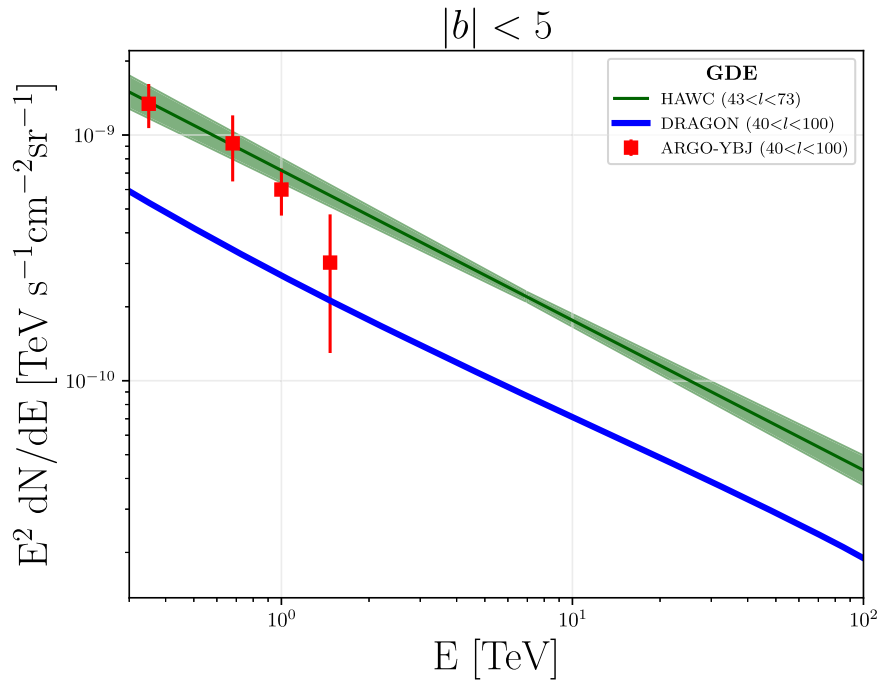**Figure 12.** Spectra of the GDE measured by HAWC and ARGO-YBJ in $|b| < 5°$ and in $43° < l < 73°$ and $40° < l < 100°$, respectively (Bartoli et al. 2015) and estimated with DRAGON within $|b| < 5°$ and $40° < l < 100°$.

Appendix C
DRAGON

The DRAGON code (Evoli et al. 2008, 2017) solves the CR transport equation accounting for diffusion, reacceleration, advection, energy losses, and spallation onto the interstellar gas. A conventional approach in which the diffusion coefficient is assumed to be isotropic in the whole Galaxy and homogeneous in the Galactic plane is chosen here. The reference setup (base model) is presented in Fornieri et al. (2020), where it was shown to reproduce the CR proton, helium, and electron spectra measured by AMS, and at larger energies relevant here, CREAM (Yoon et al. 2017) as well as the CALET (Adriani et al. 2019) results.

As mentioned in the introduction, this requires a spectral hardening in the primary nuclei spectra at an energy of $\sim 300\,\mathrm{GeV}\,\mathrm{n}^{-1}$. For the same model, DRAGON predicts both the spatial and energy distribution in the whole Galaxy for all relevant CR species which are, then, convolved with the proper cross sections and target gas/radiation distributions to determine the line-of-sight integrated gamma-ray fluxes due to π^0 decay, IC, and bremsstrahlung at each point of the sky.

For the H_2 and HI, HII, and helium gas components the same distributions adopted in the GALPROP code (Vladimirov et al. 2011) are assumed. The H_2 is based on the observed CO emission maps in several Galactocentric rings (Bronfman et al. 1988) after multiplication by a radial dependent CO-to-H_2 conversion factor which, following (Gaggero et al. 2015), is assumed to be $1.9(5) \times 10^{20}$ $(\mathrm{cm}^2\,\mathrm{K}\,\mathrm{km}\,\mathrm{s}^{-1})^{-1}$ for Galactocentric radii smaller (larger) than 7.5 kpc. The lower value is in agreement with several astrophysical measurements (Bolatto et al. 2013) while the larger value at large radii provides an effective compensation of the otherwise too steep longitude profile of the GDE (*gradient problem*) as assumed in other related works (see, e.g., Strong & Mattox 1996).

The base model is tuned to reproduce the morphology and the spectrum of the diffuse emission originated by CRs as measured by AMS in the sky window under consideration.

ORCID iDs

V. Baghmanyan ⬤ https://orcid.org/0000-0003-0477-1614
E. Belmont-Moreno ⬤ https://orcid.org/0000-0003-3207-105X
C. Brisbois ⬤ https://orcid.org/0000-0002-5493-6344
K. S. Caballero-Mora ⬤ https://orcid.org/0000-0002-4042-3855
A. Carramiñana ⬤ https://orcid.org/0000-0002-8553-3302
E. De la Fuente ⬤ https://orcid.org/0000-0001-9643-4134
M. A. DuVernois ⬤ https://orcid.org/0000-0002-2987-9691
M. Durocher ⬤ https://orcid.org/0000-0003-2169-0306
J. C. Díaz-Vélez ⬤ https://orcid.org/0000-0002-0087-0693
K. Engel ⬤ https://orcid.org/0000-0001-5737-1820
C. Espinoza ⬤ https://orcid.org/0000-0001-7074-1726
K. L. Fan ⬤ https://orcid.org/0000-0002-8246-4751
N. Fraija ⬤ https://orcid.org/0000-0002-0173-6453
A. Galván-Gámez ⬤ https://orcid.org/0000-0001-5193-3693
M. M. González ⬤ https://orcid.org/0000-0002-5209-5641
J. A. Goodman ⬤ https://orcid.org/0000-0002-9790-1299
B. Hona ⬤ https://orcid.org/0000-0002-7609-343X
D. Huang ⬤ https://orcid.org/0000-0002-5447-1786
V. Joshi ⬤ https://orcid.org/0000-0003-4467-3621
D. Kieda ⬤ https://orcid.org/0000-0003-4785-0101
A. Lara ⬤ https://orcid.org/0000-0001-6336-5291
H. León Vargas ⬤ https://orcid.org/0000-0001-5516-4975
J. T. Linnemann ⬤ https://orcid.org/0000-0003-2696-947X
A. L. Longinotti ⬤ https://orcid.org/0000-0001-8825-3624
G. Luis-Raya ⬤ https://orcid.org/0000-0003-2810-4867
K. Malone ⬤ https://orcid.org/0000-0001-8088-400X
O. Martinez ⬤ https://orcid.org/0000-0001-9052-856X
E. Moreno ⬤ https://orcid.org/0000-0002-1114-2640
M. Mostafá ⬤ https://orcid.org/0000-0002-7675-4656

L. Nellen ⬤ https://orcid.org/0000-0003-1059-8731
D. Rosa-González ⬤ https://orcid.org/0000-0003-1327-0838
K. Tollefson ⬤ https://orcid.org/0000-0001-9725-1479
I. Torres ⬤ https://orcid.org/0000-0002-1689-3945
F. Ureña-Mena ⬤ https://orcid.org/0000-0002-2748-2527
E. Willox ⬤ https://orcid.org/0000-0002-6623-0277
C. de León ⬤ https://orcid.org/0000-0002-8528-9573
D. Gaggero ⬤ https://orcid.org/0000-0003-3534-1406
D. Grasso ⬤ https://orcid.org/0000-0001-7761-7242

References

Abdalla, H., Abramowski, A., Aharonian, F., et al. 2018, A&A, 612, A1
Abdo, A. A., Allen, B., Aune, T., et al. 2008, ApJ, 688, 1078
Abeysekara, A., Albert, A., Alfaro, R., et al. 2023, NIMPA, 1052, 168253
Abeysekara, A. U., Albert, A., Alfaro, R., et al. 2017a, ApJ, 843, 40
Abeysekara, A. U., Albert, A., Alfaro, R., et al. 2017b, ApJ, 843, 39
Abeysekara, A. U., Albert, A., Alfaro, R., et al. 2017c, ApJ, 841, 100
Abeysekara, A. U., Albert, A., Alfaro, R., et al. 2019, ApJ, 881, 134
Abramowski, A., Aharonian, F., Ait Benkhali, F., et al. 2014, PhRvD, 90, 122007
Acero, F., Ackermann, M., Ajello, M., et al. 2016, ApJS, 223, 26
Ackermann, M., Ajello, M., Atwood, W. B., et al. 2012, ApJ, 750, 3
Adriani, O., Barbarino, G. C., Bazilevskaya, G. A., et al. 2011, Sci, 332, 69
Adriani, O., Akaike, Y., Asano, K., et al. 2019, PhRvL, 122, 181102
Aguilar, M., Aisa, D., Alpat, B., et al. 2015, PhRvL, 115, 211101
Aguilar, M., Ali Cavasonza, L., Ambrosi, G., et al. 2018, PhRvL, 120, 021101
Aharonian, F. A., Akhperjanian, A. G., Barrio, J. A., et al. 2001, A&A, 375, 1008
Aharonian, F. A., Akhperjanian, A. G., HEGRA Collaboration, et al. 2002, APh, 17, 459
Ahn, H. S., Allison, P., Bagliesi, M. G., et al. 2010, ApJL, 714, L89
Albert, A., Alfaro, R., Alvarez, C., et al. 2020, ApJ, 905, 76
Alemanno, F., An, Q., Azzarello, P., et al. 2021, PhRvL, 126, 201102
Amenomori, M., Bao, Y. W., Bi, X. J., et al. 2021, PhRvL, 126, 141101
An, Q., Asfandiyarov, R., Azzarello, P., et al. 2019, SciA, 5, eaax3793
Atkins, R., Benbow, W., Berley, D., et al. 2003, ApJ, 595, 803
Bartoli, B., Bernardini, P., Bi, X. J., et al. 2015, ApJ, 806, 20
Berezinskii, V. S., Bulanov, S. V., Ginzburg, V. L., Dogel, V. A., & Ptuskin, V. S. 1984, Astrophysics of Cosmic Rays (Moscow: Izdatel'stvo Nauka)
Bolatto, A. D., Wolfire, M., & Leroy, A. K. 2013, ARA&A, 51, 207
Bronfman, L., Cohen, R. S., Alvarez, H., May, J., & Thaddeus, P. 1988, ApJ, 324, 248
Cao, Z., Aharonian, F., An, Q., et al. 2023, PhRvL, 131, 151001
Cataldo, M., Pagliaroli, G., Vecchiotti, V., & Villante, F. L. 2020, ApJ, 904, 85
Evoli, C., Gaggero, D., Grasso, D., & Maccione, L. 2008, JCAP, 2008, 018
Evoli, C., Gaggero, D., Vittino, A., et al. 2017, JCAP, 2017, 015
Fornieri, O., Gaggero, D., & Grasso, D. 2020, JCAP, 2002, 009
Gaggero, D., Grasso, D., Marinelli, A., Urbano, A., & Valli, M. 2015, ApJL, 815, L25
Hanisch, R. J., Farris, A., Greisen, E. W., et al. 2001, A&A, 376, 359
Huentemeyer, P., BenZvi, S., Dingus, B., et al. 2019, BAAS, 51, 109
Hunter, S. D., Bertsch, D. L., Catelli, J. R., et al. 1997, ApJ, 481, 205
Lipari, P. 2018, APh, 97, 197
Pothast, M., Gaggero, D., Storm, E., & Weniger, C. 2018, JCAP, 2018, 45
Steppa, C., & Egberts, K. 2020, A&A, 643, A137
Stone, E. C., Cummings, A. C., McDonald, F. B., et al. 2013, Sci, 341, 150
Strong, A. W., Bloemen, J. B. G. M., Dame, T. M., et al. 1988, A&A, 207, 1
Strong, A. W., & Mattox, J. R. 1996, A&A, 308, L21
The Cherenkov Telescope Array Consortium, Acharya, B. S., Agudo, I., et al. 2017, Science with the Cherenkov Telescope Array (Singapore: World Scientific)
Thoudam, S., & Horandel, J. R. 2012, MNRAS, 421, 1209
Vecchiotti, V., Pagliaroli, G., & Villante, F. L. 2022, CmPhy, 5, 161
Vianello, G., Lauer, R. J., Younk, P., et al. 2015, arXiv:1507.08343
Vladimirov, A., Digel, S., Jóhannesson, G., et al. 2011, CoPhC, 182, 1156
Wilks, S. S. 1938, Ann. Math. Stat., 9, 60
Yang, R., Aharonian, F., & Evoli, C. 2016, PhRvD, 93, 123007
Yoon, Y. S., Anderson, T., Barrau, A., et al. 2017, ApJ, 839, 5